

aLENS: towards the cellular-scale simulation of motor-driven cytoskeletal assemblies

Wen Yan,^{1,*} Saad Ansari,² Adam Lamson,^{1,2} Matthew A. Glaser,² Meredith Betterton,² and Michael J. Shelley^{1,3}

¹*Center for Computational Biology, Flatiron Institute, New York, USA*

²*Department of Physics, University of Colorado Boulder, Boulder, USA*

³*Courant Institute, New York University, New York, USA*

(Dated: September 20, 2021)

The cytoskeleton – a collection of polymeric filaments, molecular motors, and crosslinkers – is a foundational example of active matter, and in the cell assembles into organelles that guide basic biological functions. Simulation of cytoskeletal assemblies is an important tool for modeling cellular processes and understanding their surprising material properties. Here we present *aLENS*, a novel computational framework to surmount the limits of conventional simulation methods. We model molecular motors with crosslinking kinetics that adhere to a thermodynamic energy landscape, and integrate the system dynamics while efficiently and stably enforcing hard-body repulsion between filaments – molecular potentials are entirely avoided in imposing steric constraints. Utilizing parallel computing, we simulate different mixtures of tens to hundreds of thousands of cytoskeletal filaments and crosslinking motors, recapitulating self-emergent phenomena such as bundle formation and buckling, and elucidating how motor type, thermal fluctuations, internal stresses, and confinement determine the evolution of active matter aggregates.

I. INTRODUCTION

Living systems are built hierarchically, where smaller structures assemble themselves into larger functional ones. Such organization is fundamental in life, seen across scales from molecules to organelles to cells to tissues to organisms. An example is the cellular cytoskeleton, made up of polymer filaments (and other accessory proteins) crosslinked by motor proteins that exert forces by walking processively along filaments [1]. Cellular organelles such as the cortex, spindle complex, and cilia and flagella, underlie cell polarity, division, and movement [2–5] and are assembled from the cytoskeleton. Cytoskeletal components have been reconstituted outside of cells to study self-organization in simpler settings [6, 7], and to create new active materials [8]. How cytoskeletal structures assemble from their molecular components remains challenging, especially with the wide variety of motors and crosslinkers having different behaviors on the filaments. Its understanding would allow us to predict how molecular perturbations change cell behavior and to design new complex and adaptive materials [9–11].

Computational modeling of the cytoskeleton has elucidated principles of self-organization, suggested hypotheses for experimental test, and helped interpret results of experiments [12–16]. Several software packages for cytoskeletal modeling are currently available, including Cytosim [17], MEDYAN [18], AFINES [19], and CyLaKS [20]. Cytoskeletal systems are large, with cell- and sample-sizes having 10^4 – 10^7 or more filaments [21]. While current simulations may reach $O(10^4$ – $10^5)$ filaments [22, 23], significant compromises are made in treating steric interactions and motor-protein modeling.

Here we describe computational methods and software – *aLENS* (a Living ENsemble Simulator) – designed to more efficiently and accurately simulate large cytoskeletal systems (Fig. 1). Since motor proteins must bind, crosslink, and unbind from filaments to evolve such systems, *aLENS* simulates motors as traversing a (well-defined) free energy landscape [24]. This prevents artificial energy fluxes during crosslinking processes and maintains detailed balance in the passive limit. As motors crosslink filaments, the spacing between filaments are on the order of the free length of motor proteins (10–100 nm) (Fig. 1A), comparable to filament diameters. Consequently, steric interactions between filaments are incessant and must be treated carefully to avoid unphysical stresses and deformations (Fig. 1B). Most other methods use repulsive pairwise potentials, but this limits simulations to short timescales when using stiff potentials because of the instability of timestepping methods [25]. Instead, we utilize our recent constraint method to enforce hard-core repulsion between particles [26, 27], and introduce a related constraining method to treat stiff crosslink spring forces, both of which are incorporated in a unified implicit solver. This approach ensures temporal integration stability and allows for timesteps two or more orders of magnitude larger than otherwise. Finally, *aLENS* is parallelized with OpenMP and MPI to reach length and timescales comparable to experiments (Fig. 2 and 4).

As an illustration of *aLENS*, Fig. 1C (and movie Intro.mp4) shows a modestly sized simulation of 3200 microtubules (a polar cytoskeletal filament) within a spherical volume driven by 3 times as many dynein motors that, when bound,

* wyan@flatironinstitute.org

walk to the microtubule minus-end. Though initially unorganized (C1), the combination of motor crosslinking and walking causes the microtubule minus-ends to contract into the center of a large aster (C2). The motor-driven steric interactions between filaments, however, eventually fragment this into smaller asters and bottle-brush-like structures (C3,C4). This simulation displays the complex interplay between steric and crosslink forces in determining the dynamics and steady state configurations of cytoskeletal materials.

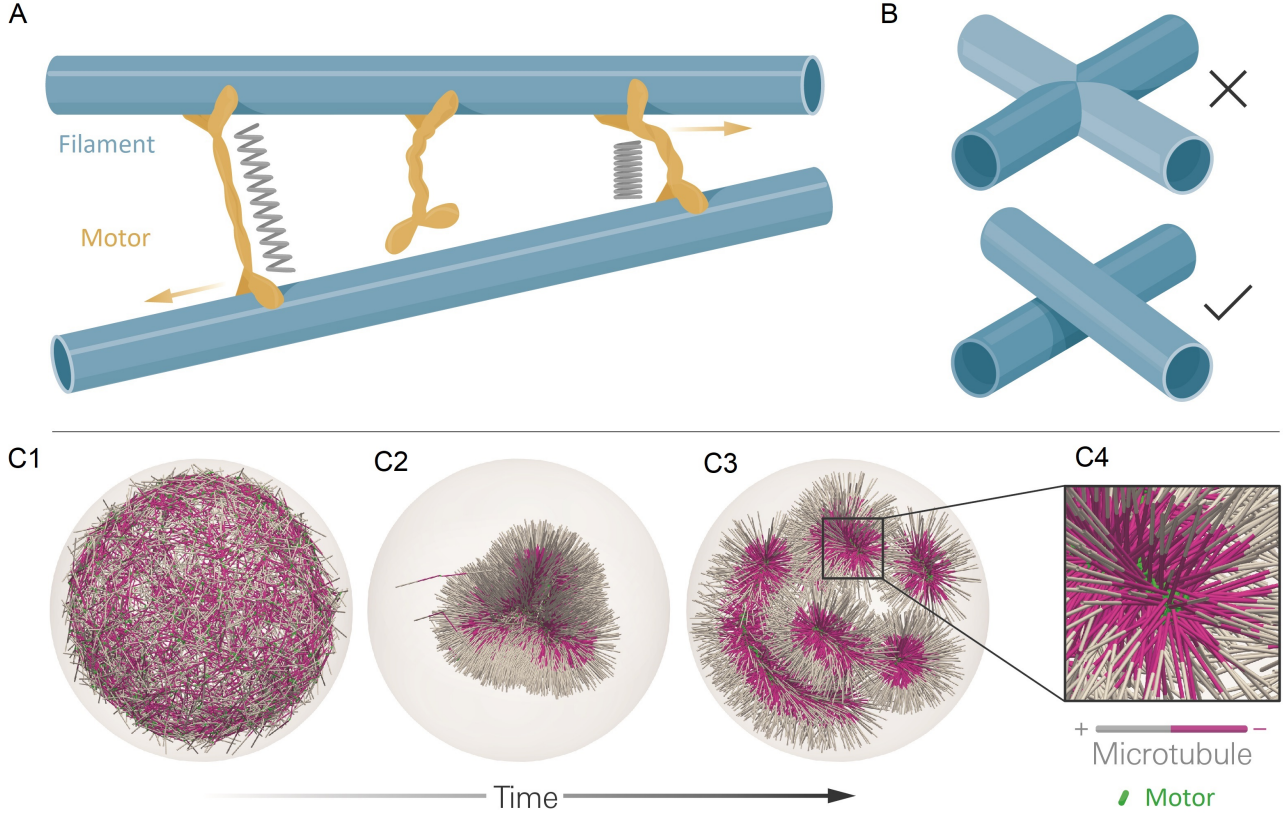


FIG. 1. **A:** *aLENS* simulates dynamics of rigid filaments crosslinked and driven by motors, thermal fluctuations, and steric interactions. Motors bind to, unbind from, and walk along filaments. **B:** To achieve high efficiency, *aLENS* computes motor forces implicitly, and steric interactions through a novel geometric constraint method that avoids filament overlaps. **C1-C3:** Example simulation of microtubules organized into asters by minus-end-directed motors. The 300 s Brownian simulation contains 3200 microtubules, each 1 μm long, inside a sphere of radius 3 μm . The initial position of each microtubule is random and the half of each filament on the minus-end is colored pink. Three end-pausing dynein motors are fixed at the minus-end of each microtubule and walk toward the minus-end of any microtubule they crosslink. After initial contraction into a single large aster, strong steric interactions in the aster center break up the system into several smaller asters and a bottle-brush structure. **C4:** Motors are highly concentrated at the centers of asters.

II. METHODOLOGY

We model filaments as rigid spherocylinders in this work, but flexible filaments can be easily assembled by chains of short, rigid segments with a defined extension and bending rigidity at each joint. Crosslinkers are modeled as Hookean spring tethers connecting two binding domains referred to as heads, with interactions between crosslinkers neglected.

As outlined below, our algorithm performs 3 tasks sequentially at every timestep. The major computational challenges arise in Task 2: computing the kinetics of crosslinkers while maintaining realistic macroscopic statistics, and in Task 3: overcoming stiffness constraints and maintaining steric exclusion, so as to reach experimental timescales of seconds or even minutes. The timestep is determined by the shortest characteristic timescale in the simulated system (filament collision, crosslinker binding/unbinding kinetics, and filament Brownian motion). All other degrees of freedom (e.g., internal conformational changes of crosslinker heads) are assumed to equilibrate on shorter timescales.

A. Task 1. Crosslinker diffusion and stepping:

Each unbound crosslinker executes Brownian motion independently. Each bound crosslinker updates the filament information it attaches to, because filaments have moved at the end of the previous timestep. Then, singly bound crosslinkers move $v_m \Delta t$ and doubly bound crosslinkers move $v_F \Delta t$ along the filaments. v_F is the tether-force-dependent walking velocity [28]:

$$v_F(F_{\text{proj}}) = v_m \max(0, \min(1, 1 + F_{\text{proj}}/F_{\text{stall}})), \quad (1)$$

where F_{proj} is the projection of tether force along the stepping direction. This formulation means if F_{proj} is assisting the stepping, the velocity saturates at v_m ; while for F_{proj} against the stepping, stepping is halted when $F_{\text{proj}} = -F_{\text{stall}}$.

B. Task 2. Crosslinker binding and unbinding kinetics:

Process	Rate	Value
$U \rightarrow (S_A, S_B)$	$R_{\text{on},s}(\mathbf{x})$	$\frac{3\epsilon K_a}{4\pi r_{c,s}^3} \sum_i L_{\text{in},i}(\mathbf{x})$
$(S_A, S_B) \rightarrow U$	$R_{\text{off},s}$	$k_{\text{o},s}$
$(S_A, S_B) \rightarrow D$	$R_{\text{on},d}(s_i)$	$k_{\text{o},d} \epsilon K_e \sum_j \int_{L_j} ds_j \exp[-(1-\lambda)\beta E(\ell_f(s))]$
$D \rightarrow (S_A, S_B)$	$R_{\text{off},d}(s_i, s_j)$	$k_{\text{o},d} \exp[\lambda E(\ell_f)]$

TABLE I. The transition rates between all possible states of a crosslinker $U \rightleftharpoons (S_A, S_B) \rightleftharpoons D$. (S_A, S_B) means either head A or B is bound but the other is unbound. All binding rates account for the linear binding density ϵ . $L_{\text{in},i}(\mathbf{x}_i, \mathbf{p}_i, \mathbf{x})$ is the length of filament i with center-of-mass position \mathbf{x}_i and orientation \mathbf{p}_i inside the capture sphere with cutoff radius $r_{c,s}$ relative to position of motor/crosslinker \mathbf{x} . The sum is over all possible candidate filaments i . The unbound-singly bound transition $U \rightleftharpoons (S_A, S_B)$ is determined by the association constant K_a and the force-independent off rate $k_{\text{o},s}$. Similarly, the singly bound-doubly bound transition $(S_A, S_B) \rightleftharpoons D$ is determined by the association constant K_e and force-independent off rate $k_{\text{o},d}$. $\beta = 1/(k_B T)$ is the Boltzmann factor. $E(\ell)$ in the $(S_A, S_B) \rightleftharpoons D$ transition rates refers to the tether energy of a motor $E(\ell) = \frac{1}{2} \kappa_{\text{xi}} (\ell_f - \ell_0)^2$. ℓ_0 is the free length of a motor, while ℓ_f is the length for computing the force when attached to filaments i and j at locations s_i and s_j : $\ell_f(s_i, s_j, \mathbf{x}_i, \mathbf{p}_i, \mathbf{x}_j, \mathbf{p}_j)$. The dimensionless factor λ determines the energy dependence in the unbinding rate. Both binding and unbinding rates must depend on λ and $k_{\text{o},d}$ such that the equilibrium constant recovers the Boltzmann factor $\exp[-\beta E(\ell_f)]$. For force-dependent binding models, the $E(\ell)$ can be simply replaced by the tether force $F(\ell)$. This is not used for results shown in this work, but implemented in the code.

In filament networks, the spatial variation of unbound and bound motors is important to network self-organization. For example, crosslinking proteins concentrate in volumes with the high filament densities, producing ripening effects as passive crosslinkers are depleted from the bulk [29] (e.g. see Fig. 1C). Furthermore, if motors or crosslinkers bind, unbind, or diffuse at rates not set by free energy barriers, the system's energy and/or entropy is artificially elevated or lowered, changing the system dynamics and steady-state configurations. Experiments have shown that entropic forces bundle and increase overlaps among crosslinked filaments [30, 31], and that free energy-dependent binding kinetics contribute to organization of cortical microtubules [32] and induce actin bundling [33].

Ad-hoc models, like those that attach crosslinkers to filaments at a fixed length or randomly sample a uniform distribution to set the binding length, are unlikely to recover the force or final configuration of bundled filaments. For example, if static crosslinkers are only allowed to bind in a non-stretched configuration, they will not generate binding entropic forces and not prefer overlapped bundles like those seen in [30]. For crosslinkers that bind with a uniform length distribution and zero tether rest length, the contractile stress of networks will be over estimated, condensing filament networks with greater rapidity.

We require that our model correctly recapitulates the distribution and chemical kinetics of crosslinking proteins in the passive limit, i.e., when $v_m = 0$ for the bound velocity of motor heads. The assemblies of filaments/crosslinkers are assumed to explore an underlying free energy landscape, where all ‘fast’ degrees of freedom can be subsumed into an effective free energy that depends only on filament and crosslinker degrees of freedom. We achieve this with a kinetic Monte Carlo procedure where crosslinking protein binding and unbinding events are modeled as stochastic processes. Transition rates recover the correct limiting (equilibrium) distribution by imposing a detailed balance requirement (SM §2). That is, we make a modeling choice to have binding and unbinding be passive processes, but it is in principle possible that certain such processes consume chemical energy.

To enforce the macroscopic thermodynamic statistics, including correct equilibrium bound-unbound concentrations and distributions (SM §2) [28, 32, 34], we explicitly model each crosslinker as a Hookean spring tether with two

binding heads labeled as A or B . Each crosslinker has 4 possible states: both heads unbound (U), either A or B (singly) bound (S_A or S_B), or both heads (doubly) bound (D). For each timestep Δt , we first calculate the rates $R(t)$ at which each head (A and B) transitions from their current state to a new binding state (i.e. for the transitions $U \rightleftharpoons (S_A, S_B) \rightleftharpoons D$). The transition probabilities are modeled as inhomogeneous Poisson processes with the cumulative probability function

$$P(\Delta t) = 1 - \exp \left(- \int_0^{\Delta t} R(t) dt \right) = 1 - \exp(-R(0)\Delta t + O(\Delta t^2)). \quad (2)$$

The transitions $U \rightleftharpoons (S_A, S_B)$ do not deform the tether for unbound or singly bound states and so does not depend on tether deformation energy. However, the transitions $(S_A, S_B) \rightleftharpoons D$ do account for tether deformation energy (Table I).

C. Task 3. Filament dynamics:

There are two stability restrictions on the timestep Δt when integrating filament velocities. One arises from using stiff repulsive pairwise potentials to prevent filament overlaps. For example, the popular Lennard-Jones potential $V \sim (\sigma/r)^{12} - (\sigma/r)^6$, where r is the separation between filaments, is so restrictive on Δt that soft alternatives such as harmonic potentials are often used [17]. These soft alternatives allow partial overlaps, and may lead to large errors in system dynamics and measured stresses [25].

The other restriction arises from the crosslinkers' fast relaxation times. When crosslinkers connect two parallel microtubules, tether lengths ℓ_f follows the relaxation ODE $\dot{\ell}_f = -\lambda(\ell_f - \ell_0)$, where ℓ_0 is the free length and $\lambda = N\kappa_{\text{xl}}/(4\pi\eta L/\log(2L/D_{\text{fil}}))$ [1]. Explicit timestepping schemes require $\Delta t < 1/\lambda$. For $N = 10$ crosslinkers, the tether stiffness $\kappa_{\text{xl}} \approx 100 \text{ pN } \mu\text{m}^{-1}$, and the slender body drag coefficient being $4\pi\eta L/\log(2L/D_{\text{fil}}) \approx 0.003 \text{ pN s } \mu\text{m}^{-1}$ for $1 \mu\text{m}$ -long microtubules in aqueous solvent, we have $1/\lambda \approx 3 \times 10^{-6} \text{ s}$.

We overcome these difficulties with a novel, linearized implicit Euler timestepping scheme, which extends on our previous work on enforcing non-overlap conditions [27]. This technique is inspired by constraint-based methods for granular flow [35]. When collisions occur between filaments, the minimal distance between them $\Phi_{\text{col}} = 0$ with collision force $\gamma_{\text{col}} > 0$. If not colliding, $\Phi_{\text{col}} > 0$ and $\gamma_{\text{col}} = 0$. This mutually exclusive condition is called a complementarity constraint, written as $0 \leq \Phi_{\text{col}} \perp \gamma_{\text{col}} \geq 0$. If one crosslinker connects these two filaments, its length ℓ_f and force magnitude γ_{xl} satisfy the Hookean spring model $\gamma_{\text{xl}} = -\kappa_{\text{xl}}(\ell_f - \ell_0)$, which is an equality constraint.

We integrate the equation of motion such that these two types of constraints for all possible collisions and all doubly bound crosslinkers are satisfied. We briefly derive the method here, and all details can be found in SM §2. The method is general to rigid particles with arbitrary shape, and we shall use ‘particle’ and ‘filament’ interchangeably.

Each particle is tracked by its center location $\mathbf{x} \in \mathbb{R}^3$ in the lab frame and its orientation $\boldsymbol{\theta} = [s, \mathbf{p}] \in \mathbb{R}^4$ as a quaternion [36]. The geometric configuration at time t for all N filaments can be written as a column vector with $7N$ entries:

$$\mathbf{C}(t) = [\mathbf{x}_1, \boldsymbol{\theta}_1, \dots, \mathbf{x}_N, \boldsymbol{\theta}_N]^T \in \mathbb{R}^{7N}. \quad (3)$$

Similarly, we use $\mathbf{U}, \mathbf{F} \in \mathbb{R}^{6N}$ to represent the translational & angular velocities, and forces & torques of all particles. The kinematic equation of motion maps \mathbf{U} to $\dot{\mathbf{C}}(t) = \partial \mathbf{C} / \partial t$, via a geometric matrix \mathbf{G} :

$$\dot{\mathbf{C}}(t) = \mathbf{G}\mathbf{U}, \quad \mathbf{U} = \mathbf{M}\mathbf{F}, \quad (4)$$

where $\mathbf{M} \in \mathbb{R}^{6N \times 6N}$ is the mobility matrix dependent on the geometry \mathbf{C} only, because the biological filaments we consider mostly have lengths on the nm to μm scales and inertia effects can be ignored.

In the following, the subscript c refers to constraints, which includes both unilateral (with subscript u) and bilateral (with subscript b) constraints. For our problem, unilateral constraints refer to collision constraints while bilateral constraints refer to crosslinker constraints. The subscript nc refers to non-constraint.

For unilateral constraints, we define the grand distance vector $\boldsymbol{\Phi}_u = [\Phi_{u,1}, \Phi_{u,2}, \dots, \Phi_{u,N_u}]^T \in \mathbb{R}^{N_u}$, where each $\Phi_{u,j}$ is the minimal distance between a pair of filaments. Similarly, for bilateral constraints we define the grand distance vector $\boldsymbol{\Phi}_b = [\ell_{f,1}, \ell_{f,2}, \dots, \ell_{f,N_b}]^T \in \mathbb{R}^{N_b}$, containing the length $\ell_{f,j}$ of the doubly bound crosslinker j . There are in total N_u possibly colliding pairs of filaments and N_b doubly bound crosslinkers. The force magnitude corresponding to these constraints are also written as vectors, $\boldsymbol{\gamma}_u = [\gamma_{u,1}, \gamma_{u,2}, \dots, \gamma_{u,N_u}]^T \in \mathbb{R}^{N_u}$ and $\boldsymbol{\gamma}_b = [\gamma_{b,1}, \gamma_{b,2}, \dots, \gamma_{b,N_b}]^T \in \mathbb{R}^{N_b}$. The two types of constraints can be summarized as:

$$\begin{aligned} 0 \leq \boldsymbol{\Phi}_u(\mathbf{C}) \perp \boldsymbol{\gamma}_u \geq 0, \\ \mathcal{K}[\boldsymbol{\Phi}_b(\mathbf{C}) - \boldsymbol{\Phi}_b^0] = -\boldsymbol{\gamma}_b. \end{aligned} \quad (5)$$

Here Φ_u and γ_u satisfy the complementarity (collision) constraints. Φ_b and γ_b satisfy the Hookean spring law. $\mathcal{K} \in \mathbb{R}^{N_b \times N_b}$ is a diagonal matrix consisting of all the stiffness constant, while Φ_b^0 represents the free length of every crosslinker.

Eqs. (4) and (5) define a differential-variational-inequality (DVI). This is solvable when closed by a geometric relation mapping the force magnitude γ_u and γ_b to the force vectors \mathcal{F}_u and \mathcal{F}_b :

$$\mathcal{F}_u = \mathcal{D}_u \gamma_u, \quad \mathcal{F}_b = \mathcal{D}_b \gamma_b, \quad (6)$$

where \mathcal{D}_u and \mathcal{D}_b are sparse matrices containing the orientation norm vectors of all constraint forces ([26, 37] and SM).

Next, we discretize this DVI using the linearized implicit Euler timestepping scheme with $\Delta t = h$ at timestep k :

$$\frac{1}{h}(\mathcal{C}^{k+1} - \mathcal{C}^k) = \mathcal{G}^k \mathcal{U}^k, \quad \mathcal{U}^k = \mathcal{M}^k (\mathcal{F}_u^k + \mathcal{F}_b^k + \mathcal{F}_{nc}^k), \quad (7a)$$

$$\mathcal{F}_u^k = \mathcal{D}_u^k \gamma_u^k, \quad \mathcal{F}_b^k = \mathcal{D}_b^k \gamma_b^k, \quad (7b)$$

$$0 \leq \Phi_u^{k+1} \perp \gamma_u^k \geq 0, \quad (7c)$$

$$\mathcal{K}^k [\Phi_b^{k+1} - \Phi_b^0] = -\gamma_b^k. \quad (7d)$$

The unknowns to be solved at every timesteps are the constraint (collision and crosslinker tether) force magnitude γ_u^k, γ_b^k . This is a nonlinear DVI because $\Phi_u^{k+1}, \Phi_b^{k+1}$ are nonlinear functions of geometry \mathcal{C}^{k+1} , although \mathcal{C}^{k+1} is linearly dependent on γ_u^k and γ_b^k . For a small timestep ($h \rightarrow 0$), this nonlinearity can be linearized by Taylor expansion, for example, $\Phi_u^{k+1} = \Phi_u^k + h \nabla_{\mathcal{C}} \Phi_u \mathcal{G}^k \mathcal{U}^k$. Then, this nonlinear DVI can be converted to a convex quadratic programming [38] (details in SM):

$$\min_{\gamma} f(\gamma^k) = \frac{1}{2} \gamma^{k,T} \mathcal{M}^k \gamma^k + \mathbf{q}^{k,T} \gamma, \quad (8a)$$

$$\text{subject to } [\mathbf{I}^{N_u \times N_u} \quad \mathbf{0}] \gamma^k \geq 0. \quad (8b)$$

Here $\gamma^k = [\gamma_u^k, \gamma_b^k] \in \mathbb{R}^{N_u + N_b}$ is a column vector, and

$$\mathcal{M}^k = \begin{bmatrix} \mathcal{D}_u^{k,T} \\ \mathcal{D}_b^{k,T} \end{bmatrix} \mathcal{M}^k [\mathcal{D}_u^k \quad \mathcal{D}_b^k] + \begin{bmatrix} 0 & 0 \\ 0 & \frac{1}{h} \mathcal{K}^{k,-1} \end{bmatrix}, \quad \mathbf{q} = \begin{bmatrix} \frac{1}{h} \Phi_u^k + \mathcal{D}_u^{k,T} \mathcal{M}^k \mathcal{F}_{nc}^k \\ \frac{1}{h} (\Phi_b^k - \Phi_b^0) + \mathcal{D}_b^{T,k} \mathcal{M}^k \mathcal{F}_{nc}^k \end{bmatrix}. \quad (9)$$

One way to understand the constraint optimization method is that the implicit temporal integration ‘jumps’ on a timescale that bypasses the relaxation timescales of unilateral and bilateral constraints (collisions and crosslinker springs). In the limit of crosslinkers being infinitely stiff ($\mathcal{K}^{-1} \rightarrow \mathbf{0}$), the quadratic term coefficient matrix \mathcal{M} is still symmetric-positive-semi-definite (SPSD) and the Eq. (8) is still convex and can be efficiently solved. Physically speaking, in this case the bilateral constraints degenerate from deformable springs to non-compliant joints.

D. Instantiation in a massively parallel computing environment:

Our methods naturally lend themselves to high-performance parallel computing architectures. We utilize both MPI and OpenMP and use standard spatial domain decomposition to balance the number of crosslinkers and filaments across MPI processors. The crosslinker update step samples the vicinity of every crosslinker, where we use a parallel near neighbor detection algorithm and update all crosslinkers in parallel. The most expensive part is the solution of Eq. (8), because its dimension is very large, equal to the total number of close pairs of filaments plus the number of crosslinked proteins. We use a fully parallel Barzilai-Borwein Projected Gradient Descent (BBPGD) solver [27], because the gradient $\nabla f = \mathcal{M} \gamma + \mathbf{q}$ is efficiently computed by one parallel sparse matrix-vector multiplication operation.

III. RESULTS

The interplay between microscopic dynamics and macroscopic order is one of the most striking features of active assemblies. We illustrate this using *aLENS* by studying the formation and extension of microtubule bundles, the polarity sorting of short microtubules on a spherical shell, the development of aster “gases” with and without thermal fluctuations, and the effect of confinement on assembling cytoskeletal structures. All simulations are conducted in solvent with viscosity $\eta = 0.01 \text{ pN s } \mu\text{m}^{-2}$ at room temperature, using a fixed timestep $\Delta t = 10^{-4} \text{ s}$ unless otherwise stated.

A. Self-aligning and buckling networks

Previous experimental studies show that microtubule networks driven by crosslinking motors can bundle and fracture dynamically [7, 39, 40]. We study such phenomena through a large-scale simulation of 100,000 filaments modeling microtubules and 500,000 motors modeling dynein motor proteins; see Fig. 2. Motor crosslinking drives an initial contraction of an initially disordered mass of bundled filaments (Fig. 2A and B). Aligning steric and crosslinking forces drive the system into a series of well-aligned bundles spanning several filament lengths (Fig. 2C and movie Buckl.mp4). In this stage, the motors move filaments parallel to each other, generating macroscopic extensile motion. Eventually, the extended network buckles and eventually fractures (Fig. 2C).

The macroscopic stresses and dynamics of such assemblies depend on the spatial organizations of filaments and crosslinking motors' behaviors. We quantify the system's organization by the joint probability distributions of a local nematic order parameter S_{local} and the number N_d of neighboring filaments crosslinked to a filament (Fig. 2D). While the network contracts, the distribution of N_d doesn't change significantly because the number of motors per filament and the maximum number of neighboring filaments within a densely packed structure remain roughly constant. However, the distribution S_{local} does change as filaments align to become near perfect nematic structures ($S_{\text{local}} \approx 1$) punctuated by less ordered regions between aligned bundles of different orientations (Fig. 2C1, D2).

Inside bundles, filaments are transported along the local nematic direction by motors. Projecting filament trajectories onto the lab-frame x -axis, we observe left- and right-moving filaments speeding up early in the simulation, and then maintaining constant average velocities at later times ($t > 4$ s in Fig. 2E), as filaments align due to steric and crosslinker forces (Fig. 2F). Note that velocity and stresses plateau only when the system's nematic order saturates.

The filament motions created by motors cause the densely-packed filaments collide often, creating a net extensile stress along the bundles' axes (Fig. 2F). However, the fixed simulation box size hinders the networks' elongation, causing the bundles aligned with x -axis to buckle from the net extensile stress (Fig. 2F, see movie Buckle.mp4). In contrast, bundles not aligned with the x -axis are not constrained and so evolve into straight spikes. This misalignment of bundles is seen as a small net stress in the y, z -directions for $t \geq 4$ s (Fig. 2F).

B. Polarity sorting in a spherical shell

The interplay between the polarity of motors and polarity of filaments drives interesting phenomena, for example, polarity sorting wherein filaments are transported to regions of like polarity. This has been well-studied on a planar but periodic geometry, e.g. [12]. Here, out of curiosity, we use *aLENS* to examine the effect of confinement geometry on polarity sorting. This is shown in Fig. 3 where 100,000 polar filaments, with aspect ratio $L/D_{\text{fil}} = 10$, are confined between two closely spaced concentric spherical shells at a high volume fraction of 40%. The shell gap is $\Delta R = 0.102$ μm , shorter than the filament length, with $\Delta R/D_{\text{fil}} \approx 4$ so filaments can move over each other in a restricted way. The filaments are initialized such that the nematic directors are along the meridians everywhere. The geometry is designed to explore the polarity sorting phenomena where the initial nematic state may interplay with the spherical geometry and significantly affect the development and steady state. 200,000 motors, modeled after Kinesin-5 tetramers, are simulated to drive the filaments' motion (Fig. 3A). Brownian motion is modeled at room temperature 300 K and timestep Δt is set to 1×10^{-5} s. Motors move towards minus ends of bound filaments at $v_m = 1.0 \mu\text{m s}^{-1}$. Once they reach the minus ends, they immediately detach and search for candidate filaments.

Motors continuously walk along the nematic directors and transport the filaments along the nematic directors (Fig. 3B). Later on, this motion 'purifies' the polarity in arctic and antarctic regions, as shown in Fig. 3C1, where filaments' orientation \mathbf{p} almost all point to the poles while those with reversed initial polarity are transported to the equatorial region. In contrast to the periodic planar geometry case [12], we did not observe the formation of 'polar lanes', where boundaries between polarity-sorted regions are mostly parallel with the polarity vectors. Instead, we find that boundaries between polarity-sorted regions are mostly orthogonal to the polarity directions, as more clearly revealed by the polarity divergence (Fig. 3C1). This clearly shows the difference of this spherical geometry from the planar case.

As the filaments are transported, motors also accumulate in some regions according to the filament polarity (Fig. 3C1). These motor accumulation regions are actually regions where the divergence of filament polarity field is positive (Fig. 3C2 and C5). This accumulation is more quantitatively revealed by the correlation function between motor number density n and $\nabla \cdot \mathbf{p}$ at $t = 4$ s in Fig. 3D. Further, motor accumulation regions may also have lower filament volume fraction (Fig. 3C2 and C4), as is shown by the correlation statistics in Fig. 3F.

This correlation between motor number density and filament polarity divergence or filament volume fraction can be understood with the schematic Fig. 3G. Once polarity sorted regions of filaments form, as the blue arrows represent, $\nabla \cdot \mathbf{p} > 0$ in regions where minus-ends meet minus-ends and vice versa in regions where plus-ends meet plus-ends. Therefore, minus-end directed motors naturally accumulate in regions with $\nabla \cdot \mathbf{p} > 0$, while plus-end motors would

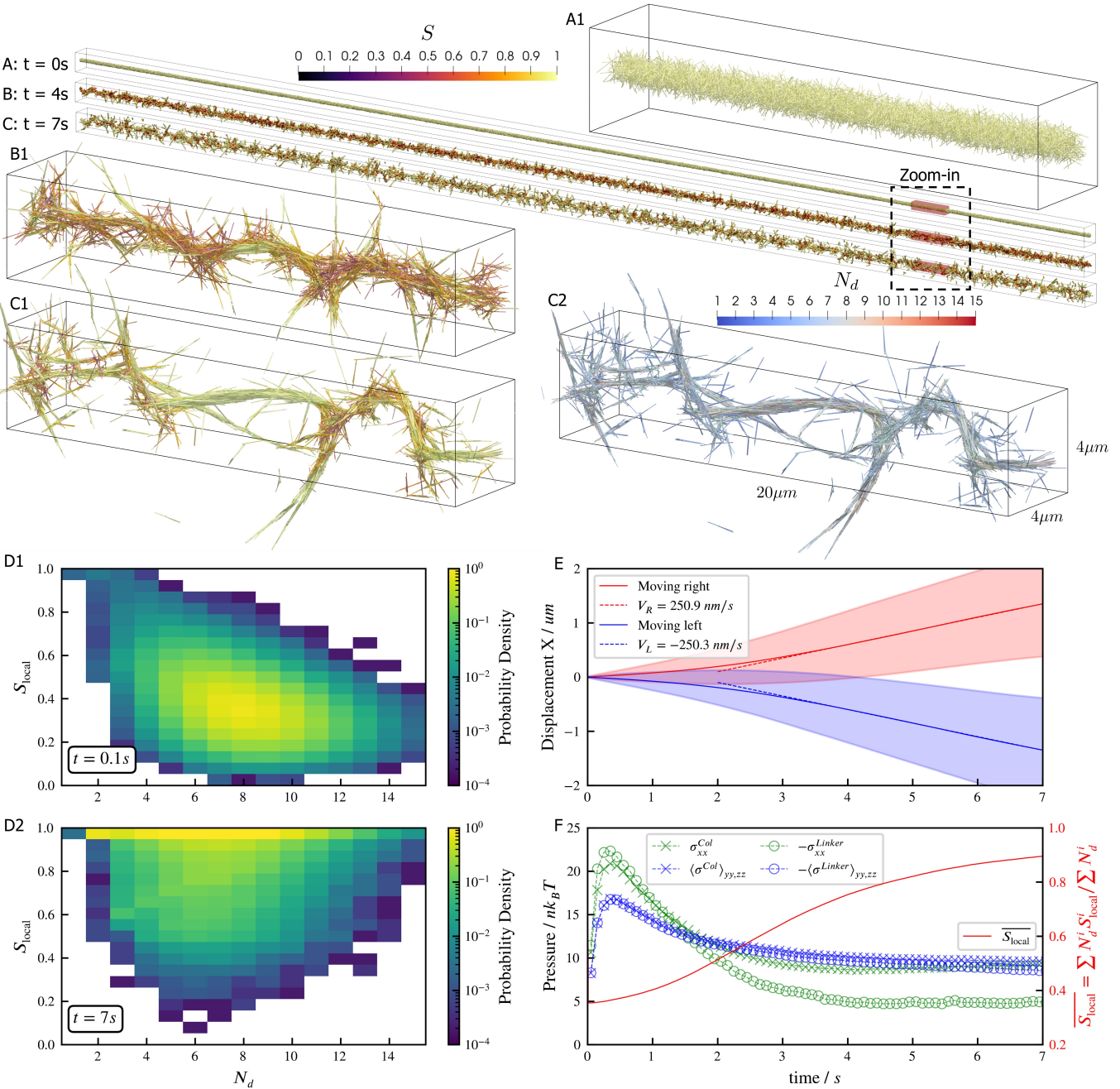


FIG. 2. Results for the bundling-buckling simulation of 100,000 microtubules and 500,000 dynein motors in the periodic simulation box of $600 \times 10 \times 10 \mu\text{m}$. Brownian motion of microtubules is turned off. Each dynein has one non-motile head permanently attached to a microtubule and the other motile head walks processively with maximum velocity $1 \mu\text{m s}^{-1}$. If bound, the motile head moves towards the microtubule minus-end, and detaches upon reaching it. Detailed parameters for this motor are tabulated in the SM §1. Every microtubule has 5 dynein motors permanently attached to randomly chosen, fixed locations along the length. The initial configuration of microtubules is randomly generated, with their orientations sampled from an isotropic distribution and centers uniformly distributed within a cylinder of length $600 \mu\text{m}$ and diameter $0.3 \mu\text{m}$. The motile heads of all dynein motors are unbound initially. **A, B, and C:** The bundle at $t = 0\text{s}$, 4s , and 7s . Microtubules are colored by their local nematic order parameter $S_{\text{local}} = \sqrt{\frac{3}{2} Q_{ij} Q_{ij}}$, with $Q_{ij} = \langle \mathbf{p}_i \mathbf{p}_j \rangle - \frac{1}{3} \delta_{ij}$, \mathbf{p} being the unit orientation vector of each microtubule pointing from the minus to the plus end, and δ the Kronecker delta tensor. The average $\langle \cdot \rangle$ is taken over each microtubule plus all microtubules that are directly crosslinked to it by dynein motors. **A1, B1, and C1:** Zoom-in views of the small region marked by red box in A, B, and C. **C2:** The same region in C1 but colored by N_d , the number of microtubules averaged over when computing S_{local} . **D1 and D2:** The joint probability distributions S_{local} and N_d for each microtubule for the entire systems at $t = 0.1\text{s}$, when the dyneins crosslink microtubules but microtubules barely move from initial configuration, and at $t = 7\text{s}$, when the bundle is nematic. **E:** The average trajectories (solid lines) and their standard deviation (shaded area) of left-moving and right-moving microtubules. Dashed lines show linear fits to the average trajectory after $t = 4\text{s}$, with results $V_R \approx V_L \approx 250 \text{ nm s}^{-1}$. **F:** The normal stresses and the weighted average \bar{S}_{local} over time. Due to the symmetry in the y, z directions, only their average is shown $\langle \sigma \rangle_{yy,zz} = \frac{1}{2} (\sigma_{yy} + \sigma_{zz})$. Collision stress is positive (extensile) and crosslinker stress is negative (contractile). The weighted average $\bar{S}_{\text{local}} = \sum N_d^i S_{\text{local}}^i / \sum N_d^i$.

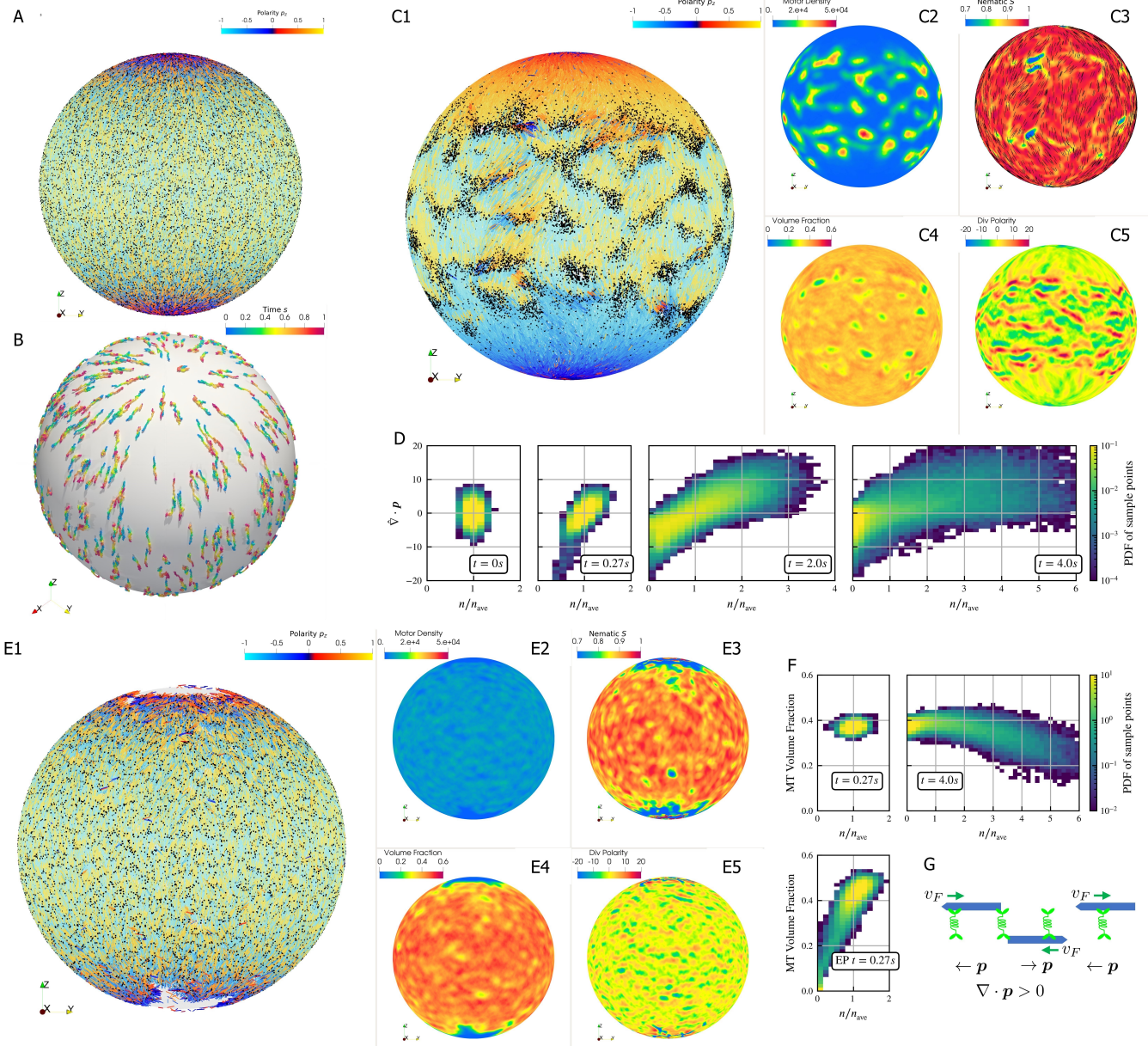


FIG. 3. Results for the polarity sorting simulation in a spherical shell. Initially, 100,000 $0.25 \mu\text{m}$ -long filaments modeling microtubules and 200,000 motors modeling crosslinking kinesin-like proteins are placed between two concentric spherical shells with radii $r_{\text{in}} = 5 \mu\text{m}$ and $r_{\text{out}} = 5.102 \mu\text{m}$, to maintain the volume fraction of filaments between these two shells at 40%. Initially, all filaments are evenly distributed on the spherical shell, with their orientation randomly chosen to be either $\pm \mathbf{e}_\theta$ at each point, where \mathbf{e}_θ is the polar basis norm vector of spherical coordinate system. The pure filament system is relaxed for 1 s to resolve the overlaps in the initial configuration. Afterwards at $t = 0$, 200,000 motors are added to the system homogeneously distributed between the two shells. Sample points are evenly placed to measure the statistics by averaging the volume within $0.25 \mu\text{m}$ from each sample point. **A:** The configuration at $t = 0$. Filaments are colored by their polarity, while motors are colored as black dots. Only randomly selected 10% of all motors (same after) are shown in the image to illustrate the distribution. **B:** Randomly selected trajectories of filaments from $t = 0$ s to 1 s. Trajectories are colored by time. It is clear that filaments move along the meridians. **C1-C5:** Configuration and statistics at $t = 4$ s. **C1:** The filaments and motors. Motors clearly concentrate in some areas. **C2:** The motor number density, i.e., number of motors per $1 \mu\text{m}^3$. **C3:** The nematic director field (shown as black bars) and the nematic order parameter S . **C4:** The filament volume fraction. **C5:** The divergence of polarity field $\nabla \cdot \mathbf{p}$ non-dimensionalized by filament length, i.e., change of mean polarity per filament length. **D:** The development of the correlation between motor number density n/n_{ave} and the polarity divergence field, at different times of the simulation. Clearly high n/n_{ave} are correlated with positive polarity divergence. **E1-E5:** Configuration and statistics at $t = 0.27$ s for a comparative simulation where motors have end-pausing, arranged in the same style as **C1-C5**. This case shows significant contraction instead of polarity sorting as filaments are pulled away from the north and south poles and the overall volume fraction significantly increases to approximately 60%. The structure becomes densely packed and does not significantly evolve further. **F:** The correlation between motor number density n/n_{ave} and the local filament volume fraction. For the polarity sorting case at $t = 4$ s the motor number density correlates with low filament volume fraction. This is not seen in the end pausing (EP) case. **G:** A schematic for the correlations shown in **D** and **F**.

accumulate in regions with $\nabla \cdot \mathbf{p} < 0$. Once motors accumulate, they may attach to both minus ends and push them away such that the distance between minus ends is preferably the free length of motors. As a result, the sampled volume fraction of filaments in that region is below average.

In contrast, if the motors stop walking but do not detach when they reach the minus ends (end-pausing, EP), the system quickly contracts to a densely packed network (Fig. 3E1-5) with volume fraction increases from 40% to 60% and seems to stop evolving at $t = 0.27$ s. We observe neither substantial polarity sorting nor motor accumulation. This indicates that the ability of motors to continuously walk, without end-pausing, is crucial to effective polarity sorting.

C. Aster formation in bulk

If instead of walking off of filament ends, motors linger there (known as end-pausing), cytoskeletal networks tend to form aster-like structures instead of nematic ones. Most studies have focus on how motor details drive aster formation [22, 40]. Here we investigate the effects of thermal fluctuations. In two simulations, we evolve 40,000 filaments and 80,000 processive, minus-end-directed, end-pausing motors starting from the same spatially uniform and orientationally isotropic random configuration (Fig. 4A). In one, filaments move stochastically under thermal fluctuations (Fig. 4D and movie BMT_Aster.mp4), while the second is athermal (retaining stochasticity of free motors and binding) (Fig. 4E and movie NBMT_Aster.mp4). Thermal fluctuations significantly influence the asters' shape, structure, and ultimate spatial organization. The BMT simulation shows a system of dispersed, spherically symmetric, dense asters. Comparatively, the NBMT simulation shows a larger number of regularly-spaced but irregularly-shaped asters containing fewer filaments (Fig. 4D vs E).

Asters form when crosslinking motors reorganize filaments so that their minus ends are clustered and held tight by paused motors. Fig. 4B shows the radial distribution function $g(r)$ of all minus ends. In both BMT and NBMT simulations, two prominent peaks emerge in $g(r)$ at small length scales $r = 25$ nm = D_{fil} and $r = 78$ nm = $\ell_0 + D_{\text{fil}}$ which correspond to lengths where filaments touch or are crosslinked by motors, respectively (Fig. 4B, D2, E2). The relatively small peak between these two maxima correspond to filaments that are “geometrically confined” between two crosslinked filaments. On larger length scales, $g(r)$ for BMTs indicates larger and denser asters than those of NBMTs. Non-Brownian filaments do not move unless two filaments are close enough to become crosslinked. This suggests that, at steady state, NBMT aster centers are separated by twice the individual filament length. In contrast, Brownian filaments may diffuse ~ 1 μm in 1 s. This allows free filaments to be captured by regions of high motor density, i.e., aster centers. Furthermore, BMT asters also diffuse, which leads to asters sporadically coalescing (Fig. 4D1). These observations and estimated lengthscale are quantitatively confirmed by analyzing the static structure factor of aster centers (details in SM §4), which shows that the NBMT case has smaller, but approximately 3 times more, asters than the BMT case (Fig. 4D vs E).

The differences in the dynamics of aster formation are also reflected in stress measurements (Fig. 4C), where the more crowded filament configurations of the BMT case produces a much larger stress throughout the simulation. In both cases Π^{Linker} initially increases quickly, reaching a peak at roughly $t = 4$ s ~ 5 s, similar to the behavior during bundle contraction in the previous section (Fig. 2F), before declining. The average processive walking time of the motors from attachment to the filament ends, $\tau_{\text{walk}} = L/v_m \approx 5$ s, characterizes this timescale. After reaching minus ends, motors pause and relax towards their equilibrium lengths. Both crosslinker and collision stresses grow in magnitude as more motors congregate at minus ends.

D. Confined filament-motor protein assemblies

In vivo, cytoskeletal filaments are spatially constrained by encompassing membranes, organelles, and other cellular structures. Whereas in the previous part we explored how filaments and end-pausing motors assemble into asters in an open geometry, here we now confine a similar system to the inside of an open cylinder with periodic boundary conditions. That the cylinder surface is a hard boundary to motors and filaments is easily implemented within our complementarity constraints.

Figure 5 shows simulations for 0.25 μm long filaments at a fixed packing fraction ($\phi = 0.16$), confined in two cylinders with diameters $D_{\text{cyl}} = 0.25$ μm and 0.75 μm . Similar to the previous bulk cases, motors create high-density crosslinked filament aggregates that coexist with a relatively low density vapor of non-crosslinked filaments. In bulk systems, crosslinked aggregates tend to form asters because the combined action of crosslinking and walking pulls filament ends together. We find that a confining cylindrical boundary strongly modifies the conformation of these aggregated structures, as shown in Fig. 5.

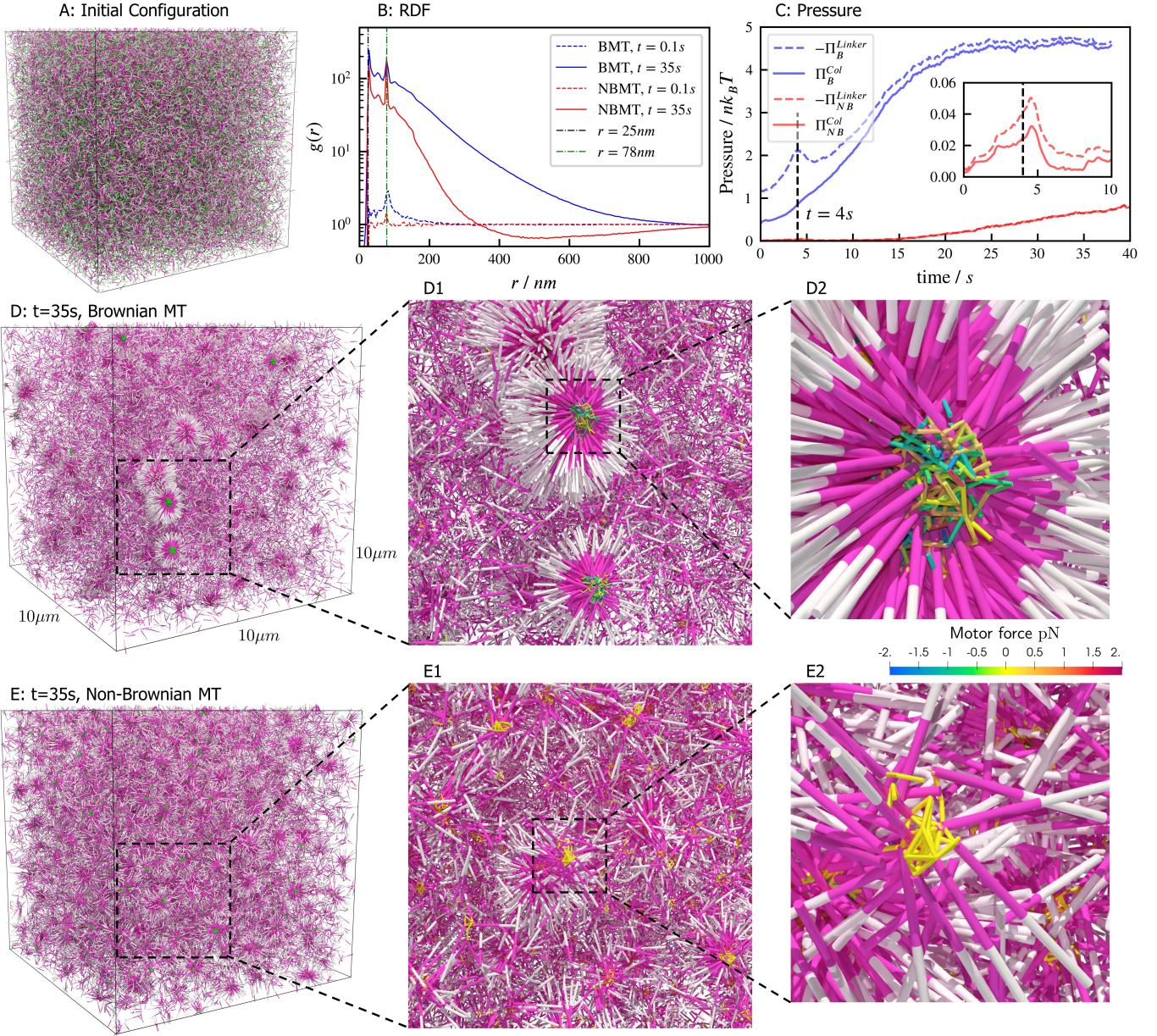


FIG. 4. Results for the aster formation simulations with Brownian motion of simulated microtubules turned on (BMT) and off (NBMT). Initially, 40,000 0.5 μm -long filaments modeling microtubules and 80,000 motors modeling crosslinking kinesin-like proteins are placed in a periodic cubic box of $10 \times 10 \times 10 \mu\text{m}$ with uniform distribution. Filament orientations are isotropic and motors are all in the unbound state. Motors are assumed to have two minus-end-directed walking heads with symmetric properties. They are assumed to pause when they reach the minus end of filaments until detaching. Detailed parameters are tabulated in the SM §1. **A**, **D**, and **E**: Simulation snapshots. Each filament is shown as a cylinder colored in half pink (minus end) and half white (plus end). **A**: The initial configuration for both NMT and BNMT cases. Each motor is colored as a green dot. **D** and **E**: The snapshot for both cases at $t = 35\text{ s}$. **D1-2** and **E1-2**: Expanded views of a aster core for D and E. Only doubly bound motors are shown in D and E (in green color), and in D1-2 & E1-2 (colored by the spring force). Negative values mean the crosslink forces are contractile (attractive). **B**: The radial distribution function (RDF) $g(r)$ for the minus ends of all filaments at $t = 0.1\text{ s}$ (dashed lines) and $t = 35\text{ s}$ (solid lines). The first peak of $g(r)$ at $r = 25\text{ nm}$ corresponds to close contacts between filaments. The second peak of $g(r)$ at $r = 78\text{ nm} = 25\text{ nm} + 53\text{ nm}$ corresponds to the minus ends of filaments crosslinked by motors whose rest length is 53 nm. Blue and red lines are results for the BMT and NBMT cases, respectively. **C**: The collision (solid) and crosslinker (dashed) pressure for BMT (blue) and NBMT (red) cases. Pressure is defined as the trace of the stress tensor: $\Pi = \frac{1}{3}\text{Tr}\boldsymbol{\sigma}$. The collision pressure Π^{Col} is positive (extensile), and the motor pressure Π^{Linker} is negative (contractile). The inset plot shows the pressure for the NBMT case in the initial stage of the simulation. The black dashed lines mark the time $t = 4\text{ s}$.

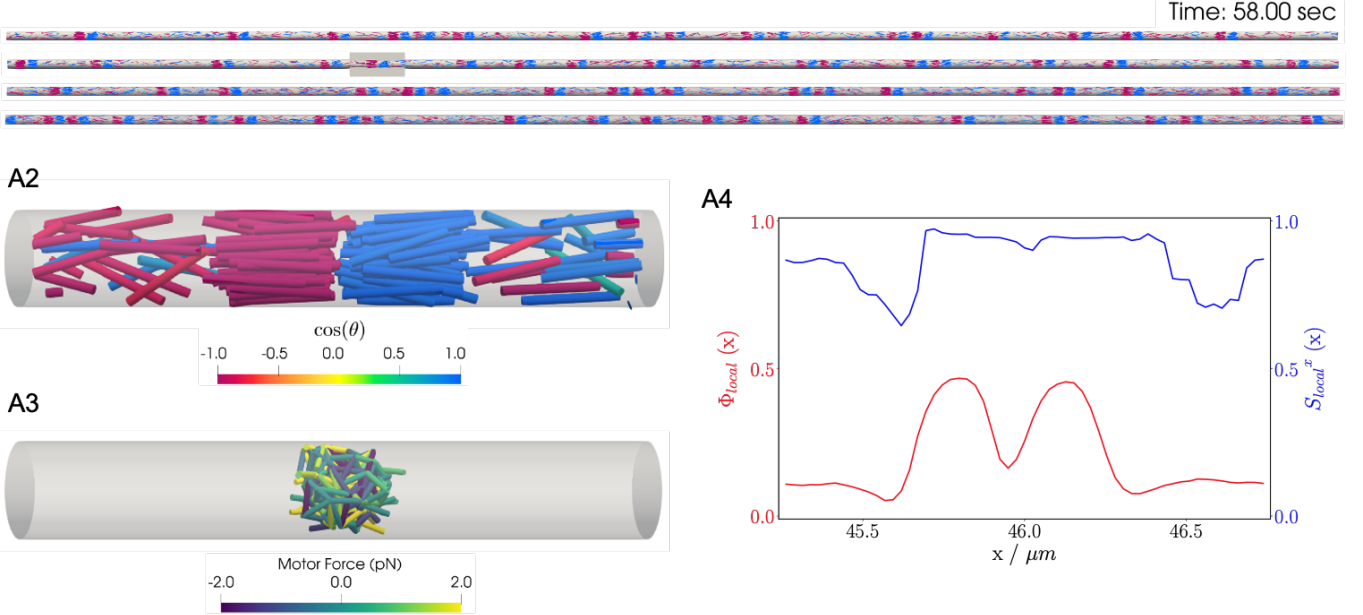
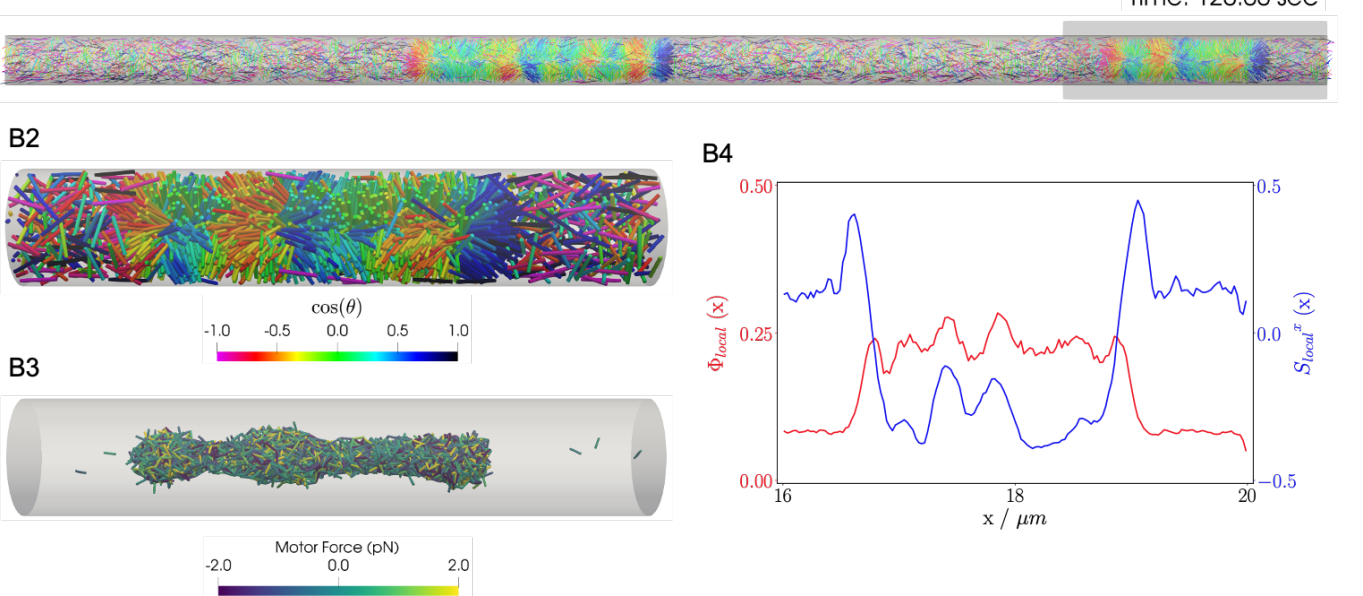
A1: Confinement Diameter = $0.25 \mu\text{m}$ B1: Confinement Diameter = $0.75 \mu\text{m}$ 

FIG. 5. Results for the confined filament-motor protein assembly simulations with 9,216 filaments modeling microtubules and 27,648 motors modeling crosslinking kinesin-like proteins at a cylinder diameter of $D_{\text{cyl}} = 0.25 \mu\text{m}$ and $0.75 \mu\text{m}$. Initially, $0.25 \mu\text{m}$ long filaments are uniformly distributed and aligned along the x -axis, with equal numbers oriented in the $+x$ and $-x$ directions. Crosslinking motor proteins are initially unbound and distributed uniformly as well. **A** and **B**: Snapshots of the simulation with $D_{\text{cyl}} = 0.25 \mu\text{m}$ and $0.75 \mu\text{m}$ at $t = 58\text{s}$ and $t = 120\text{s}$. **A1** and **B1**: All 9216 simulated filaments. In **A1**, the cylinder is too long to be displayed contiguously, therefore a stacked representation is shown. The filaments are colored by the value of $\cos \theta$ where θ is the angle between the filament direction vector \mathbf{p} (oriented from the minus-end to the plus-end) and the positive x -axis (pointing to the right). **A2** and **B2**: Zoomed-in view of the filaments in the boxed regions in **A1** and **B1**. **A3** and **B3**: Doubly-bound motors in the boxed regions, colored by their binding force. Negative values represent contractile force while positive values indicate extensile force. **A4** and **B4**: The local packing fraction (red line) and the local nematic order parameter (blue line), $S_{\text{local}}^x(x) = \sum_i^{N(x)} W_i(x) S_{\text{local}}^x(x)_i$ where a filament i contributes $S_{\text{local}}^x(x)_i = \frac{1}{2}(3 \cos^2 \theta_i - 1)$ to the local order at x . Filament contributions are weighted by $W_i(x)$ and summed over all filaments at x . Line plots represent an average over 1s for the snapshots in **A2** and **B2**. Detailed parameters, calculations, and movies for the crosslinking motor proteins are presented in the SM §1 and §5.

For the $D_{\text{cyl}} = 0.25 \mu\text{m}$ case ($D_{\text{cyl}}/L = 1$, Fig. 5A and movie pf16_d100.mp4), filaments condense into polarity-sorted bilayers (PSBs). A single PSB contains a central interface of highly-crosslinked filament minus-ends between two polar layers of filaments (Fig. 5A2-3). At steady state, the system consists of individual PSBs separated by low-density vapor regions containing few crosslinking motors. Unsurprisingly, the local nematic order parameter $S_{\text{local}}^x(x)$ almost saturates at 1 within PSBs. Even the the vapor phase is close to nematic $S_{\text{local}}^x \approx 0.6$ (Fig. 5A4), due to the strong confinement effect.

In the $D_{\text{cyl}} = 0.75 \mu\text{m}$ case ($D_{\text{cyl}}/L = 3$, Fig. 5B and movie pf16_d300.mp4), the larger diameter allows filaments to reorient and organize into bottle-brush-like aggregates (BBs) where filament plus ends are oriented radially outward from the cylinder axis, forming a hedgehog line defect capped by half asters (Fig. 5B2). Walking leaves motors highly concentrated along the line defects (Fig. 5B3) and the radial hedgehog structure of BBs is evidenced by a negative local nematic order parameter (Fig. 5B4, blue line). The splayed nature of the BBs produces a lower relative packing fraction of ~ 2.5 times the vapor when compared to the PSBs (Fig. 5B4, red line).

IV. DISCUSSION

aLENS is designed to (i) model crosslinker kinetics conforming to an underlying free energy landscape, (ii) break the timescale limitation imposed by conventional explicit timestepping methods, and (iii) efficiently utilize modern parallel computing resources to scale to cellular scale systems. More detailed timing results can be found in the SM §3. Within this efficient framework, we simultaneously track the individual building blocks of active assembly and gather mesoscale statistical information such as stress and order parameters. Such a multiscale capability makes it possible to directly compare with experimental observations on mesoscopic and macroscopic scales over timescales from seconds to minutes.

This framework is not limited to modeling rigid filaments or a specific motor/crosslinker model. Having a modular design, the crosslinking protein model can be extended conveniently to include force-dependent binding and unbinding rates, or even entirely replaced with another model for crosslinking proteins. Dynamic instability and branching of cytoskeletal filaments can also be conveniently integrated with the constraint minimization problem, as we showed previously in modeling the division-driven growth of bacterial colonies [27]. Long and flexible polymers can be also simulated by chaining short and rigid segments together with flexible connections [17], even with nonlocal interactions mediated by hydrodynamics, electrostatics, or other fields [41–43]. For example, in ongoing work we have used *aLENS* to simulate chromatin in the nucleus as a bead-spring chain moving through the nucleoplasmic fluid, and confined by the nuclear envelope.

Recent years have seen considerable innovation in computational approaches to cytoskeletal modeling, implemented in powerful simulation packages including Cytosim [17], MEDYAN [18], and AFINES [19]. These packages utilize a variety of coarse-grained representations of cytoskeletal elements and numerical simulation schemes, with the diversity of approaches in part reflecting the diversity of cytoskeletal systems and phenomena of interest. *aLENS* brings a powerful set of new capabilities to the table, significantly expanding the range of accessible time and length scales in simulations of systems in which excluded volume and crosslink-mediated interactions play a dominant role.

V. ACKNOWLEDGEMENT

MJS acknowledges support from NSF grants DMR-2004469 and CMMI-1762506. SA, ARL, MAG, and MB acknowledge support from NSF grants DMS-1821305, ACI-1532235, ACI-1532236, and NIH grant RGM124371A.

[1] J. Howard *et al.*, *Mechanics of motor proteins and the cytoskeleton*, Vol. 743 (Sinauer associates Sunderland, MA, 2001).

[2] M. Bornens, *Nature Reviews Molecular Cell Biology* **9**, 874 (2008).

[3] E. Barnhart, K.-C. Lee, G. M. Allen, J. A. Theriot, and A. Mogilner, *Proceedings of the National Academy of Sciences* **112**, 5045 (2015), <https://www.pnas.org/content/112/16/5045.full.pdf>.

[4] J. R. McIntosh, *Cold Spring Harbor perspectives in biology* **8**, a023218 (2016).

[5] T. D. Pollard and B. O’Shaughnessy, *Annual Review of Biochemistry* **88**, 661 (2019).

[6] F. J. Nedelev, T. Surrey, A. C. Maggs, and S. Leibler, *Nature* **389**, 305 (1997).

[7] P. J. Foster, S. Fürthauer, M. J. Shelley, and D. J. Needlman, *eLife* **4**, e10837 (2015).

[8] S. J. DeCamp, G. S. Redner, A. Baskaran, M. F. Hagan, and Z. Dogic, *Nature Materials* **14**, 1110 (2015).

[9] R. Li and G. G. Gundersen, *Nature Reviews Molecular Cell Biology* **9**, 860 (2008).

[10] D. A. Fletcher and R. D. Mullins, *Nature* **463**, 485 (2010).

- [11] D. Needleman and Z. Dogic, *Nature Reviews Materials* **2**, 1 (2017).
- [12] T. Gao, R. Blackwell, M. A. Glaser, M. D. Betterton, and M. J. Shelley, *Physical Review Letters* **114**, 048101 (2015).
- [13] S. A. Rincon, A. Lamson, R. Blackwell, V. Syrovatkina, V. Fraisier, A. Paoletti, M. D. Betterton, and P. T. Tran, *Nature Communications* **8**, 15286 (2017).
- [14] P. Bun, S. Dmitrieff, J. M. Belmonte, F. J. Nédélec, and P. Lénárt, *Elife* **7**, e31469 (2018).
- [15] D. Saintillan, M. J. Shelley, and A. Zidovska, *Proceedings of the National Academy of Sciences* **115**, 11442 (2018).
- [16] M. Varghese, A. Baskaran, M. F. Hagan, and A. Baskaran, *Physical Review Letters* **125**, 268003 (2020).
- [17] F. Nedelev and D. Foethke, *New Journal of Physics* **9**, 427 (2007).
- [18] K. Popov, J. Komianos, and G. A. Papoian, *PLOS Computational Biology* **12**, e1004877 (2016).
- [19] S. L. Freedman, S. Banerjee, G. M. Hocky, and A. R. Dinner, *Biophysical Journal* **113**, 448 (2017).
- [20] S. A. Fiorenza, D. G. Steckhahn, and M. D. Betterton, *bioRxiv* [10.1101/2021.03.31.437972](https://doi.org/10.1101/2021.03.31.437972) (2021), <https://www.biorxiv.org/content/early/2021/04/02/2021.03.31.437972.full.pdf>.
- [21] S. Petry, *Annual Review of Biochemistry* **85**, 659 (2016), pMID: 27145846, <https://doi.org/10.1146/annurev-biochem-060815-014528>.
- [22] J. M. Belmonte, M. Leptin, and F. Nédélec, *Molecular Systems Biology* **13**, 941 (2017), <https://www.embopress.org/doi/pdf/10.1525/msb.20177796>.
- [23] T. Strübing, A. Khosravanzadeh, A. Vilfan, E. Bodenschatz, R. Golestanian, and I. Guido, *Nano Letters* **20**, 6281 (2020).
- [24] A. R. Lamson, J. M. Moore, F. Fang, M. A. Glaser, M. J. Shelley, and M. D. Betterton, *The European Physical Journal E* **44**, 45 (2021).
- [25] D. M. Heyes and J. R. Melrose, *Journal of Non-Newtonian Fluid Mechanics* **46**, 1 (1993).
- [26] M. Anitescu, J. F. Cremer, and F. A. Potra, *Mechanics of Structures and Machines* **24**, 405 (1996).
- [27] W. Yan, H. Zhang, and M. J. Shelley, *The Journal of Chemical Physics* **150**, 064109 (2019).
- [28] T. Gao, R. Blackwell, M. A. Glaser, M. D. Betterton, and M. J. Shelley, *Physical Review E* **92**, 062709 (2015).
- [29] K. L. Weirich, S. Banerjee, K. Dasbiswas, T. A. Witten, S. Vaikuntanathan, and M. L. Gardel, *Proceedings of the National Academy of Sciences* **114**, 2131 (2017).
- [30] Z. Lansky, M. Braun, A. Lüdecke, M. Schlierf, P. R. ten Wolde, M. E. Janson, and S. Diez, *Cell* **160**, 1159 (2015).
- [31] I. Gaska, M. E. Armstrong, A. Alfieri, and S. Forth, *Developmental Cell* **54**, 367 (2020).
- [32] J. F. Allard, J. C. Ambrose, G. O. Wasteneys, and E. N. Cytrynbaum, *Biophysical Journal* **99**, 1082 (2010).
- [33] L. Yang, D. Sept, and A. Carlsson, *Biophysical Journal* **90**, 4295 (2006).
- [34] A. R. Lamson, C. J. Edelmaier, M. A. Glaser, and M. D. Betterton, *Biophysical Journal* **116**, 1719 (2019).
- [35] A. Tasora, M. Anitescu, S. Negrini, and D. Negrut, *International Journal of Non-Linear Mechanics Multibody System Dynamics: A Selective Perspective*, **53**, 2 (2013).
- [36] S. Delong, F. B. Usabiaga, and A. Donev, *The Journal of Chemical Physics* **143**, 144107 (2015).
- [37] W. Yan, E. Corona, D. Malhotra, S. Veerapaneni, and M. Shelley, *Journal of Computational Physics* **416**, 109524 (2020).
- [38] J. Nocedal and S. Wright, *Numerical Optimization*, Springer Series in Operations Research and Financial Engineering (Springer New York, 2006).
- [39] T. Sanchez, D. T. N. Chen, S. J. DeCamp, M. Heymann, and Z. Dogic, *Nature* **491**, 431 (2012).
- [40] J. Roostalu, J. Rickman, C. Thomas, F. Nédélec, and T. Surrey, *Cell* **175**, 796 (2018).
- [41] M. J. Shelley, *Annual Review of Fluid Mechanics* **48**, 487 (2016).
- [42] E. Nazockdast, A. Rahimian, D. Zorin, and M. Shelley, *Journal of Computational Physics* **329**, 173 (2017).
- [43] O. Maxian, A. Mogilner, and A. Donev, *Physical Review Fluids* **6**, 014102 (2021).